A realistic algorithm for microtubule-based nucleation reveals large sensitivity to cell geometry of the plant cortical array

Marco Saltini, Eva E. Deinum

Mathematical & Statistical Methods (Biometris), Plant Science Group, Wageningen University, 6708 PB Wageningen, The Netherlands

Keywords: computational biology, plant cortical microtubules, nucleation, event-driven simulations, biophysical modelling, CorticalSim.

Abstract

The self-organisation of cortical microtubules into aligned arrays plays a key role in plant cell morphogenesis and organismal growth. Computational studies have highlighted the impact of simulation domain topology and directional biases in microtubule dynamics on this alignment. Despite this, simulating microtubule nucleation has been challenging for years, as modelling nucleation of new microtubules from extant microtubules lead to inhomogeneity within cortical arrays, characterized by large empty spaces and few densely populated areas. We introduce a novel, efficient algorithm that realistically simulates microtubule nucleation by approximating the diffusion of nucleation complexes, which yields uniform arrays by maintaining realism in the nucleation process without the computational burden of explicit diffusion simulation. With our model, we show that strong biases towards specific orientations of alignment in self-organised arrays can emerge naturally when nucleation is modelled with enhanced biological realism. More specifically, we observe that cell geometry has a strong influence in driving the array towards a preferred transverse orientation. Our approach opens up new avenues for quantitative comparisons of different factors influencing array orientation and, as such, can be a powerful tool for re-assessing conclusions about the drivers of microtubule alignment in plant cells.

Introduction

Plants take their shape through coordinated processes of cell division, expansion and differentiation. At the cellular level, many of these processes are shaped by the plant cortical microtubule array [1–3]. This dynamic structure of membrane associated microtubules guides the anisotropic deposition of cellulose microfibrils, the main load bearing component of the cell wall, and predicts the future cell division site [4–7]. Under the right conditions [8, 9], these dynamic microtubules can self-organize into a highly aligned array. Unlike animals, plant cells organise their cortical microtubules through collisional interactions rather than through centralised organising centres [10]. The dynamics of individual microtubules, by controlling the strength of such collisional interactions, play a crucial role in this organisation. Microtubule nucleation, particularly the orientation of newly-generated microtubules in relation to their parent microtubules, is key to the self-organisation of the cortical microtubule array [11–14]. Consequently, to shed light on the dynamics of cortical microtubules, particularly concerning their self-organisation and alignment it is essential to consider realistic models for microtubule nucleation.

The state of cortical microtubule arrays is significantly influenced by a combination of global and local cues. For example, global cues such as cell geometry can favour array orientation along the shortest closed circumferences of the cell [15, 16]. Conversely, local cues, including the alignment of microtubules with mechanical stresses [17], have the potential to override global cue and select for a specific orientation for the alignment of the array [18, 19]. Given that new microtubules in plants typically nucleate in directions strongly correlated with the orientation of their parent microtubule [20–22], how microtubules are nucleated in simulations of the cortical array is crucial. Indeed, different nucleation modes result in different sensitivities to local and global cues [11, 12, 19]. Therefore, the ability to realistically simulate microtubule nucleation is critical for any computational study that involves a competition between local and global cues affecting alignment and orientation.

Despite this importance, most computational research on microtubule arrays has traditionally employed isotropic nucleation, where microtubules are initiated at random positions with random orientations. While helpful for understanding the effects of microtubule collisions [8, 10, 23] and geometrical constraints on alignment [15, 18, 24–26], this approach simplifies the actual complexity, overlooking that microtubules often nucleate from existing ones [20, 27]. Efforts to include microtubule-based nucleation in models have faced challenges, highlighting the necessity for more realistic simulation methods. Many simulation studies with microtubule-based nucleation [12,21,28,29], however, suffer from a so-called "inhomogeneity problem" [11]. This problem is a computational issue arising from a naive implementation of microtubule-based nucleation, i.e., when microtubule-based nucleation is linearly density-dependent. This density-dependence causes a positive feedback on microtubule on local microtubule density, leading to overly dense regions and very sparse areas in between. As cellulose synthase complexes are preferentially inserted near microtubules [6], such inhomogeneities would lead to structural weakness of the cell wall. While this feedback loop originates from the biological reality of microbule-based nucleation, the naive implementation has no counteracting force. In reality, however, the local nucleation rate saturates with density, thereby ensuring homogeneity [11].

Jacobs et al. [11] demonstrated that one solution to this problem is to explicitly consider the appearance and diffusion at the membrane of nucleation complexes. They implemented this in a simplified array simulation dubbed CorticalSimple, in which alignment of microtubules is taken for granted, i.e., they all have an exactly transverse orientation [11]. In CorticalSimple, nucleation complex diffusion takes up a large fraction the computational time, even though nucleation itself is

a relatively rare event. The diffusion of explicit nucleation complexes is also employed in CytoSim (e.g., [30]), in which the computational cost of diffusing "nucleators" is less problematic, because the microtubule model itself is computationally much more demanding due to its larger degree of mechanical realism. The computational load of CytoSim, however, makes it unsuitable for simulating a large number of instances of plant cortical arrays. A different platform, corticalSim, is specifically developed for this. Previous publications with corticalSim heavily use its computational efficiency, which allows for accurate computation of ensemble statistics and exploration of parameter space [12, 21, 31, 32]. The computational efficiency of corticalSim stems from its adoption of an event-driven approach for microtubule dynamics and interaction, which updates the system following each event rather than at fixed time intervals. This methodology enables simulations with a large number of repetitions, providing results of higher statistical significance. Nonetheless, incorporating the diffusion dynamics of nucleation complexes into the framework, as seen in the work by Jacobs et al. [11], has the potential to introduce a trade-off by increasing the computational cost. Therefore, in the context of corticalSim, it is necessary to develop a new nucleation mode that 1) maintains a high level of biological realism and allows for the explicit consideration of nucleation complex dynamics, 2) reproduces density-dependence nucleation of new microtubules without causing array inhomogeneity, and 3) is computationally efficient.

In this paper, we tackle these challenges by introducing a novel nucleation algorithm for CorticalSim that efficiently simulates the diffusion of nucleation complexes in a simplified manner. Our approach accounts for biologically realistic microtubule-based nucleation, enabling the natural emergence of density-dependent from the nucleation process at both local and global scales. This nucleation mode promotes the formation of aligned cortical microtubule arrays while overcoming the long-standing issue of inhomogeneity. Furthermore, we compare arrays produced by our algorithm with those generated through isotropic and previous density-dependent nucleation modes. Our findings show that realistic nucleation modes enhance the responsiveness of the array to orientational cues stemming from the cellular geometry.

Methods

The new nucleation algorithm is implemented in CorticalSim, a fast, event based microtubule simulation platform written in C++ [31]. Table 1 summarizes model parameters and their default values.

Microtubule dynamics

The dynamics of microtubules comprises two main components: intrinsic dynamics and microtubule-microtubule interaction. We employed the Dogterom and Leibler model [33] to describes the intrinsic dynamics of individual microtubules augmented with hybrid treadmilling [34], see Figure 1A. Microtubules can be either in the growing state, where they extend at the plus-end with a growth speed of v^+, or in the shrinking state, where they retract their plus-end with a shrinkage speed of v^-. The minus-end of microtubules retracts at a treadmilling speed of v^{tm} independently of the state of the plus-end. Transitions between the growing and shrinking states, and *vice versa*, occur with catastrophe and rescue rates denoted as r_c and r_r, respectively.

When a growing microtubule plus end impinges on the lattice of another microtubule, the resulting type of interaction depends on the collision angle, comprised between 0° and 90°. For

Table 1: Default model parameters.

Parameter	Description	Value	Unit
v^+	Growth speed	0.05	μm s^{-1}
v^-	Shrinkage speed	0.08	μm s^{-1}
v^{tm}	Treadmilling speed	0.01	μm s^{-1}
r_c	Catastrophe rate	variable	s^{-1}
r_r	Rescue rate	0.001	s^{-1}
θ_c	Maximum collisional angle for bundling	40°	-
P_{cat}	Fraction of induced catastrophe after collision when $\theta > \theta_c$	0.5	-
r_n	Nucleation rate for ISO and GDD	0.001	μm^{-2} s^{-1}
r_{ins}	Insertion rate for LDD	0.0045	μm^{-2} s^{-1}
r_u	Per-complex unbound nucleation rate	0.002	s^{-1}
D	Diffusion coefficient of nucleation complexes	0.013	μm^2 s^{-1}
N	Number of meta-trajectories for LDD	6	-
R	Maximum meta-trajectory length for LDD	1.5	μm
$P_{\mathrm{rej},b}$	Rejection probability for microtubule-based nucleation for LDD	0.76	-
$P_{\mathrm{rej},u}$	Rejection probability for unbound nucleation for LDD	0.98	-
$\rho_{1/2}$	Tubulin density at which half of nucleations are isotropic for GDD	0.1	μm^{-1}
f_{forward}	Nucleation probability along the parent for GDD and LDD	0.31	-
f_{backward}	Nucleation probability anti-parallel to the parent for GDD and LDD	0.07	-
f_{left}	Nucleation probability to the left of the parent for GDD and LDD	0.31	-
f_{right}	Nucleation probability to the right of the parent for GDD and LDD	0.31	-
ϵ	Ellipse eccentricity for GDD and LDD	0.89	-
θ_b	Mean branching angle for GDD and LDD	35°	-

collision angles smaller than $\theta_c = 40°$, zippering occurs, causing the plus end to reorient alongside the encountered microtubule. When the collision angle is wider than 40°, the impinging plus-end has a probability P_{cat} to undergo a collision-induced catastrophe, and a probability $1 - P_{\mathrm{cat}}$ to create a cross-over with the other microtubule, see Figure 1B. Microtubule bundles emerge as a result of the zippering process. We assume that the collision between a growing microtubule tip and a bundle is equivalent to a collision with a single microtubule. Likewise, when a microtubule within a bundle collides with another microtubule, it remains unaffected by the presence of other microtubules within the same bundle. CorticalSim can simulate microtubule severing events induced by the severing enzyme katanin [32]. However, for simplicity, we do not consider katanin severing in this manuscript.

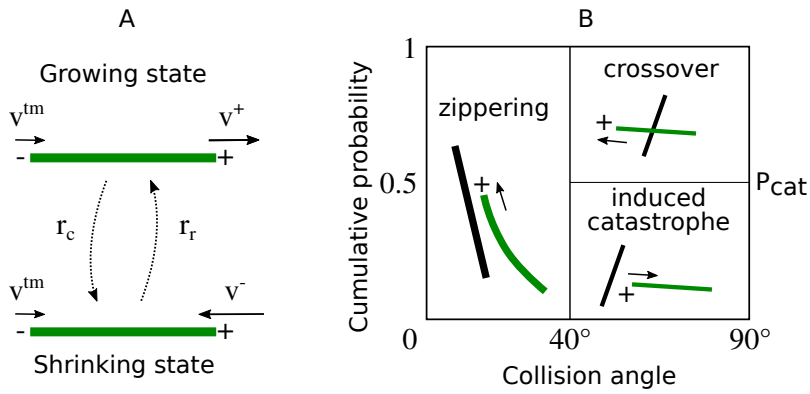

Figure 1: Schematic of the dynamics of individual microtubules. (A) Microtubules switch from periods of growth to periods of shrinkage (with catastrophe rate r_c), and *viceversa* (with rescue rate r_r). (B) Microtubule plus-ends impinging on the lattice of other microtubules with an angle lower than 40° result in zippering. For higher collision angles the result is an induced catastrophe of the impinging microtubule with probability P_{cat}, or crossover with probability $1 - P_{\text{cat}}$.

Microtubule nucleation

In plants, microtubules are nucleated from a γ-tubulin ring complex (γ-TuRC) which serves as a scaffold for the assembly of microtubules [35]. γ-TuRCs are primarily observed on the lattices of existing microtubules [14, 20, 27]. The initial growth direction of newly-nucleated microtubules often aligns with the orientation of the parent microtubule, influencing the overall alignment of the microtubule array. Consequently, the mode of nucleation plays a key role for the self-organisation and alignment of the cortical microtubule array, suggesting that variations in nucleation modes can lead to different patterns in the array.

Here, we explore three distinct modes of microtubule nucleation: isotropic nucleation, global density-dependent nucleation, and a novel local density-dependent nucleation algorithm. The latter consists of a new computational approach, and we compare its performance against the former two methods, already well-studied in the literature [21, 28, 29, 31]. Regardless of the chosen nucleation mode, we assume that nucleation complex availability is constant over time.

Isotropic. In the case of isotropic nucleation, new microtubules are nucleated at a rate r_n. The location and orientation are randomly selected with uniform probability. We hereafter refer to this nucleation mode as ISO.

Global density-dependence. In the global density-dependent nucleation (GDD) case, which was developed in [21], nucleation can be either microtubule-based or background unbound nucleation. Given the total density of tubulin ρ used by microtubules, the rate at which microtubule-based nucleation occurs is

$$r_{n,\text{MT-based}} = r_n \frac{\rho}{\rho + \rho_{1/2}}, \tag{1}$$

where $\rho_{1/2}$ is an equilibrium constant determining the density at which half of the nucleations are microtubule-based [22]. Consequently, isotropic background nucleation occurs at a rate $r_{n,\text{unbound}} = (r_n - r_{n,\text{MT-based}})$. This approach aligns with observations, ensuring that initial nucleations in the

microtubule-free membrane are unbound, while a small fraction of unbound nucleations occurs even at higher densities. In our simulations, the locations of microtubule-based nucleation events are uniformly distributed along the length of all available microtubules.

We modelled the angular distribution of microtubule-based nucleations as proposed by Deinum et al. [21]. Their nucleation mode includes three components: forward (towards the plus-end of the parent microtubule) with probability f_{forward}, backward (towards the minus-end of the parent microtubule) with probability f_{backward}, and the remaining probability sideways, split between left (f_{left}) and right (f_{right}). The sideways component are modelled by fitting elliptically shaped polar distributions to the data by Chan and Lloyd [20]. The full nucleation distribution function, denoted as $\nu(\theta)$, where θ is the angle between the direction of the parent and the daughter microtubules, combines these components:

$$\begin{aligned}\nu(\theta) = f_{\text{forward}}\delta(\theta) + f_{\text{backward}}\delta(\theta-\pi) \\ + \frac{(1-\epsilon^2)^{\frac{3}{2}}}{2\pi}\left[f_{\text{left}}\left(\frac{1}{1-\epsilon\cos(\theta-\theta_b)}\right)^2 + f_{\text{right}}\left(\frac{1}{1-\epsilon\cos(\theta+\theta_b)}\right)^2\right],\end{aligned} \tag{2}$$

where ϵ is the ellipse eccentricity, θ_b the mean branching angle, and δ the Dirac distribution.

Local density-dependence. New nucleation complexes appear at the membrane at rate r_{ins}. These complexes are placed at a random position $\mathbf{x}_0$ within the domain. For convenience, and without loss of generality, we set $\mathbf{x}_0 = (0,0)$ in the remainder of this section. To define a region for nucleation, we consider a circle with a radius R centered at $\mathbf{x}_0$, which we call the nucleation area. Within this area, we draw N radii, each referred to as a meta-trajectory. The first meta-trajectory is drawn at a random angle $\theta_1 \in [0, 2\pi)$ in the simulation domain, while subsequent meta-trajectories have angles $\theta_i = \theta_{i-1} + 2\pi/N$, see Figure 2A and B. A meta-trajectory labelled by i may either intersect the lattice of a microtubule at a distance r_i from the centre or reach the boundary of the nucleation area, with r_i being equal to the radius R in the latter case. When a meta-trajectory intersects a microtubule lattice, it stops there (Figure 2B). We approximate the diffusion process by assuming that the γ-complex can either reach these intersections by diffusion or diffuse away from the nucleation area. In our analysis, we set $N = 6$ to reasonably represent the possible directions of diffusion of γ-complexes.

In general, following an insertion, three outcomes are possible: (i) the nucleation complex dissociates, (ii) an unbound nucleation occurs, (iii) or the complex reaches the lattice of a microtubule. In the latter case, after reaching a microtubule lattice, the complex may either result in a microtubule-based nucleation or dissociate. The probability that a nucleation complex dissociates is different depending on whether such a complex was freely diffusing or attached to a microtubule lattice. In the former case, the probability of dissociation is 98%, in the latter 76% [11, 14]. Ideally, the nucleation process should be modelled as a two-stage mechanism. Nonetheless, considering the limitation that experimental data are predominantly available for dense arrays and that the rates and probabilities of dissociation are determinable only *a posteriori* [14], i.e., depending on whether a complex has reached a lattice or not, we adopt a pragmatic approach. Initially, we determine the likelihood of a complex reaching a microtubule lattice. Should this happen, within our algorithm, we schedule a microtubule-based nucleation event. If the complex does not reach a microtubule lattice, we then schedule an unbound nucleation. Subsequently, we reject scheduled nucleation events, applying the relevant rejection probabilities to ensure our model aligns with observed experimental

behaviours.

Whether a γ-complex reaches a microtubule lattice depends on a diffusion process. Indeed, it reaches a lattice if the time it takes to to do so from the moment of the insertion is shorter than the waiting time between insertion and unbound nucleation. If the time exceeds this threshold, the insertion results in an unbound nucleation, provided that the potential nucleation is not rejected. We consider this time as deterministic and derive it from the mean squared displacement of a diffusive particle in two dimensions:

$$\tau_i = \frac{d_i^2}{4D}. \tag{3}$$

The waiting time from insertion to unbound nucleation is modeled as exponentially distributed, with an unbound nucleation rate denoted as r_u. Consequently, the probability p that a microtubule reaches the lattice intersected by the meta-trajectory i before unbound nucleation is given by:

$$p(d_i) = \int_{\tau_i}^{\infty} \mathrm{d}t\, r_u e^{-r_u t} = e^{-r_u \frac{d_i^2}{4D}}. \tag{4}$$

Hence, $0.24p(d_i)$ represents the likelihood of a microtubule-based nucleation, given that meta-trajectory i was chosen. Accordingly, $0.02\,(1 - p(d_i))$ is the probability of unbound nucleation given that meta-trajectory i was chosen. In our simulations, we used a maximum meta-trajectory length of $R = 1.5\mu$m because, given our choice of parameters values (Table 1), the probability $p(R)$ of a γ-complex intersecting with a microtubule lattice prior to nucleation becomes negligible beyond this length. Based on this, the probability of microtubule-based nucleation after an insertion is

$$p_{\text{MT-based}} = \frac{0.24}{N} \sum_j p(r_j), \tag{5}$$

where the sum over j only runs over meta-trajectories that intersect a microtubule, while the probability of unbound nucleation is $0.02(1 - p_{\text{MT-based}})$, see Figure 2C. We refer to this nucleation mode as local density-dependent (LDD). Note that, for computational efficiency, one could equivalently use $r'_{\text{ins}} = r_{\text{ins}}/0.24$ and accept all possible bound nucleations and possible unbound nucleations with probability $0.83 = 0.02/0.24$.

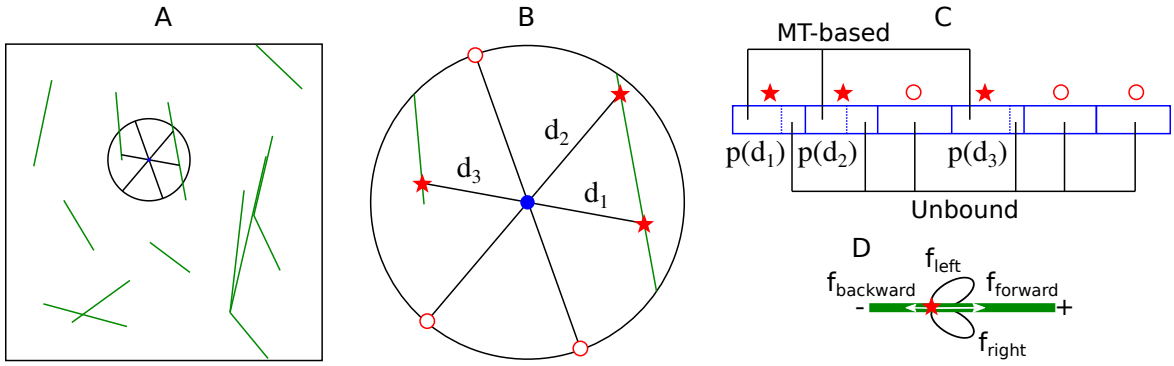

Figure 2: Schematic of the LDD nucleation algorithm. (A) An insertion position in the simulation domain is selected randomly, with uniform distribution. (B) Such a position, represented by the blue circle, is the centre of the nucleation area (the area included in the black circumference). N meta-trajectories are drawn equidistant from one another and with random orientation. Meta-trajectories are drawn up until the closer between the boundary of the nucleation area or the lattice of an intersecting microtubule. (C) Whether the resulting nucleation is microtubule-based or unbound and, in the former case, the parent microtubule and the nucleation location, is decided stochastically with probability $0.24p(r_i)$ weighted over the length of meta-trajectories, according to Equation (4). (D) In a microtubule-based nucleation, the angles follow [21]: a newly-nucleated microtubule initially grows along the parent microtubule with probability f_{forward}, in the opposite direction with probability f_{backward}, or branches to either side with probability $f_{\text{left/right}}$. The branching angle is determined according to a distribution that closely matches the data in [20].

Degree of alignment and orientation of the array

To assess the alignment of microtubules in a planar system, we use a nematic order parameter S_2 that accounts for the contribution of individual microtubule segments proportionally weighted on their length [21]. For planar geometries, S_2 is defined by

$$S_2 = \sqrt{\langle\langle \cos 2\theta \rangle\rangle^2 + \langle\langle \sin 2\theta \rangle\rangle^2}, \tag{6}$$

where the double brackets denote a length-weighted average over all microtubule segments. S_2 has a value of 0 for an isotropic system and a value of 1 for a system where microtubules are perfectly aligned. For non-planar geometries, we use the order parameter $R_2 \in [0, 1]$ which extends the definition of nematic order parameter to surfaces in the 3D space as defined in [31]. We couple the alignment order parameter S_2 with the overall array orientation Θ_2:

$$\Theta_2 = \arctan\left(\frac{\langle\langle \sin 2\theta \rangle\rangle}{\langle\langle \cos 2\theta \rangle\rangle + S_2}\right). \tag{7}$$

Similarly, for non planar geometries like a capped cylinder, it is possible to extend the definition of Θ_2 to surfaces in the 3D space [31].

Navigating parameter space with control parameter G

The driver of spontaneous alignment in the cortical array is the occurrence of sufficient interactions within the average microtubule length. This is quantified by a single control parameter G [8, 9], which is the ratio of two length scales: an interaction length scale (left factor) and the average length of non-interacting microtubules (right factor). We use a version of G adjusted for minus end treadmilling [21]:

$$G = \left(\frac{2(v^+ - v^{\mathrm{tm}})^2 (v^- + v^{\mathrm{tm}})}{r_n v^+ (v^+ + v^-)} \right)^{1/3} \left(\frac{r_r}{v^- + v^{\mathrm{tm}}} - \frac{r_c}{v^+ - v^{\mathrm{tm}}} \right). \tag{8}$$

Note that we restrict ourselves to $G < 0$, i.e., when microtubules are in the so-called bounded-growth regime, where they have a finite life span and finite intrinsic length. In this case, spontaneous alignment occurs if $G > G^*$, some threshold that depends on the details of microtubule-microtubule interactions. In graphs where we vary G, we use the notation G_c to indicate that G is varied via r_c.

For ISO and GDD nucleation modes, the nucleation rate r_n is an explicit simulation parameter. For LDD nucleation, however, r_n results from the interplay between insertion rate r_{ins} and rejection of nucleations, which in turn depends on the density and distribution of the microtubules. Therefore, we calculate the effective nucleation rate to be used for G in Equation (8) as

$$r_n = \frac{n_c(T)}{TA}, \tag{9}$$

where $n_c(T)$ is the number of nucleation events occurred after time T, and A is the area of the simulation domain. In principle, n_c might be non-linear in T, making our proposed computation of r_n overly-simplistic. However, our test showed that $n_c(T)$ is approximately linear in T, for $T < 3 \times 10^4$ seconds, see Figure S1.

Results

In this section, we used default parameter values listed in Table 1. The default simulation domain in a square grid with periodic boundary conditions and size $L = 40\mu$m. We tuned the value of the parameter G by varying the catastrophe rate r_c. The above, if not otherwise indicated, should be considered our default parameter values and the basis of our analysis.

LDD nucleation results in homogeneous aligned arrays

We first studied the self-organisation of the cortical microtubule array in two-dimensional rectangles with periodic boundary conditions, and different sizes: $L = 80\mu$m and $H = 80\mu$m, $L = 40\mu$m and $H = 40\mu$m, $L = 20\mu$m and $H = 20\mu$m, $L = 20\mu$m and $H = 40\mu$m, $L = 20\mu$m and $H = 80\mu$m. More specifically, we compared snapshots of the cortical array at $T = 3 \times 10^4$ seconds in the aligned regime, analysing arrays obtained through LDD, GDD, and ISO nucleation modes. The threshold value of the control parameter G, at which the array can be considered aligned, varies according to the size and aspect ratio of the simulation domain. This threshold was determined by measuring the degree of alignment S_2 averaged over 100 simulation runs, across the five distinct simulation domains as a function of G (Figure S2).

Figure 3 shows snapshots of aligned arrays for each studied geometry and nucleation mode. The degree of alignment S_2 of the snapshots provided accurately reflects the average degree of alignment in relation to the control parameter G (see Figure S2). The visual representation shows that simulations using the LDD mode resulted in homogeneous arrays across various geometries, akin to those obtained with the ISO mode. Partial inhomogeneity, as observed in LDD (Figure 3D), was transient, as shown in Figure S3A. Conversely, in the GDD mode, homogeneity was hardly restored or even achieved at all, as illustrated in Figure S3B. The striking difference between LDD and GDD can be attributed to the insertion of new nucleation complexes at random location throughout the simulation domain in LDD. This, in principle, can ensure that newly-nucleated microtubules are introduced more uniformly, leading to a roughly even distribution across various regions of the simulation domain and in the different bundles. In contrast, the positive feedback mechanism in GDD primarily directed new microtubules to already densely populated bundles. It could only nucleate new microtubules to sparsely populated areas through background unbound nucleation, which occurred rarely at high density, according to Equation (1).

Moreover, we observed in Figure 3A that, while homogeneity in the LDD and ISO modes was similar, there were significant differences in the level of alignment. In the former case, the alignment was higher, with $S_2 = 0.93$, compared to $S_2 = 0.84$ in ISO, see also Figure S2. This suggests that, even for large geometries, LDD could sustain an alignment of the array, likely caused by strong orientational correlations. In contrast, ISO exhibited different local ordering emerging from the simulation, partially hindering the alignment of the array.

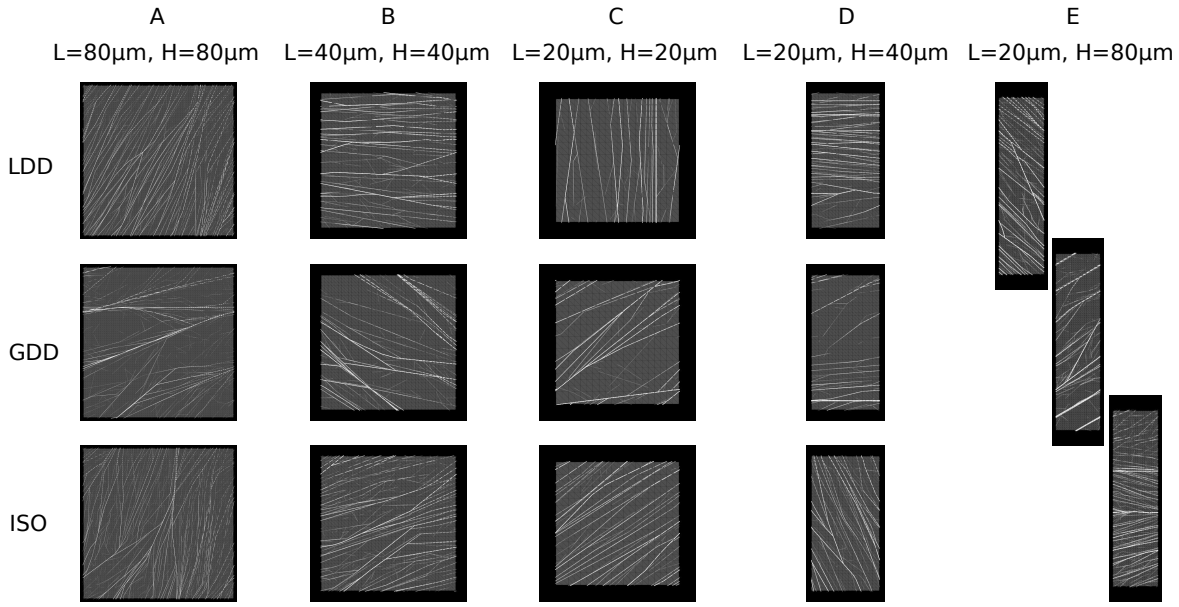

Figure 3: Snapshot of the simulation domain at $T = 3 \times 10^4$ seconds with different sizes of the domain with periodic boundary conditions. The different domain sizes are not in scale with each other for visibility.
(A) LDD: $S_2 = 0.93$, $G = -0.19$. GDD: $S_2 = 0.85$ $G = -0.27$. ISO: $S_2 = 0.84$, $G = -0.14$.
(B) LDD: $S_2 = 0.96$, $G = -0.19$. GDD: $S_2 = 0.89$, $G = -0.23$. ISO: $S_2 = 0.90$, $G = -0.14$.
(C) LDD: $S_2 = 0.97$, $G = -0.18$. GDD: $S_2 = 0.88$, $G = -0.14$, ISO: $S_2 = 0.97$, $G = -0.12$.
(D) LDD: $S_2 = 0.97$, $G = -0.19$. GDD: $S_2 = 0.95$, $G = -0.25$. ISO: $S_2 = 0.95$, $G = -0.14$.
(E) LDD: $S_2 = 0.91$, $G = -0.20$. GDD: $S_2 = 0.89$, $G = -0.27$. ISO: $S_2 = 0.83$, $G = -0.16$.

LDD nucleation increases the regime of spontaneous alignment

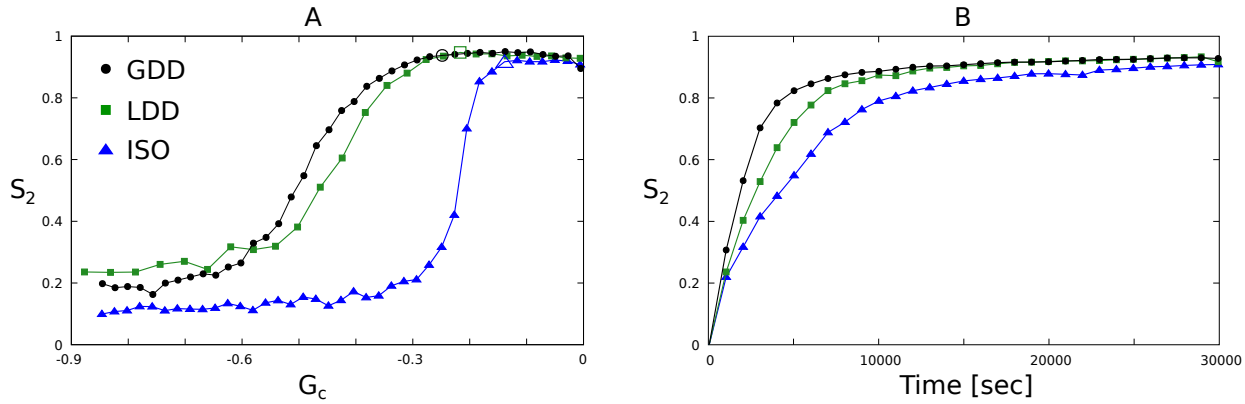

Figure 4: Order regime for LDD, GDD, and ISO nucleation modes in a squared geometry with sizes $L = 40\mu$m and $H = 40\mu$m. (A) Order parameter S_2 as function of the control parameter G at $T = 3 \times 10^4$ sec, averaged over 100 independent simulation runs. Data points marked as larger, empty circle, square, or triangle correspond to the parameter values used for panel (B). (B) Order parameter S_2 as function of the simulation time. Results are averaged over 100 independent runs for selected values of G (data points marked in red in panel (A)) in the order regime. Error bars of (A) can be found in Figure S4.

We computed the order parameter S_2 as a function of the control parameter G at $T = 3 \times 10^4$ seconds averaged over 100 simulations for LDD, GDD, and ISO nucleation modes. Figure 4A shows that, compared to ISO, LDD expanded the range of values of G such that the array was well aligned in a preferred direction, with a similar behaviour for the $S_2(G)$ curve to GDD. More specifically, the aligned regime could be achieved for roughly the same G values as in the GDD case. For intermediate values of G, although the behaviour was more comparable to GDD that it was to ISO, LDD produces a less aligned array, likely consequence of the higher number of background nucleation compared to what happened for higher G values, i.e., when more collisions occurred. Figure S2 shows that, in the LDD and ISO cases, increasing the size of the simulation domain had the potential to lower the value of the order parameter S_2 due to the creation of local ordering (see also Figure 3A). In the GDD case, this effect was less pronounced, likely due to the high probability of nucleation of new microtubules from extant microtubules in already highly populated bundles. This did not occur in ISO and LDD.

In the aligned regime, due to microtubule-based nucleation being more likely than unbound nucleation, the alignment of the array occurred at a faster pace than in the ISO case, though not as fast as in the GDD, see Figure 4B. Again, the positive feedback loop attracting the nucleation of new microtubules in densely populated bundles significantly accelerated alignment, since newly-nucleated microtubules are more likely to initially grow in a direction similar to that of their parent microtubules, as theoretically shown by Foteinopoulos and Mulder [22]. This inclination of new microtubules towards an already established preferred direction of alignment, while present in the LDD scenario, was substantially less pronounced than in GDD.

LDD is a bias-free algorithm for microtubule nucleation

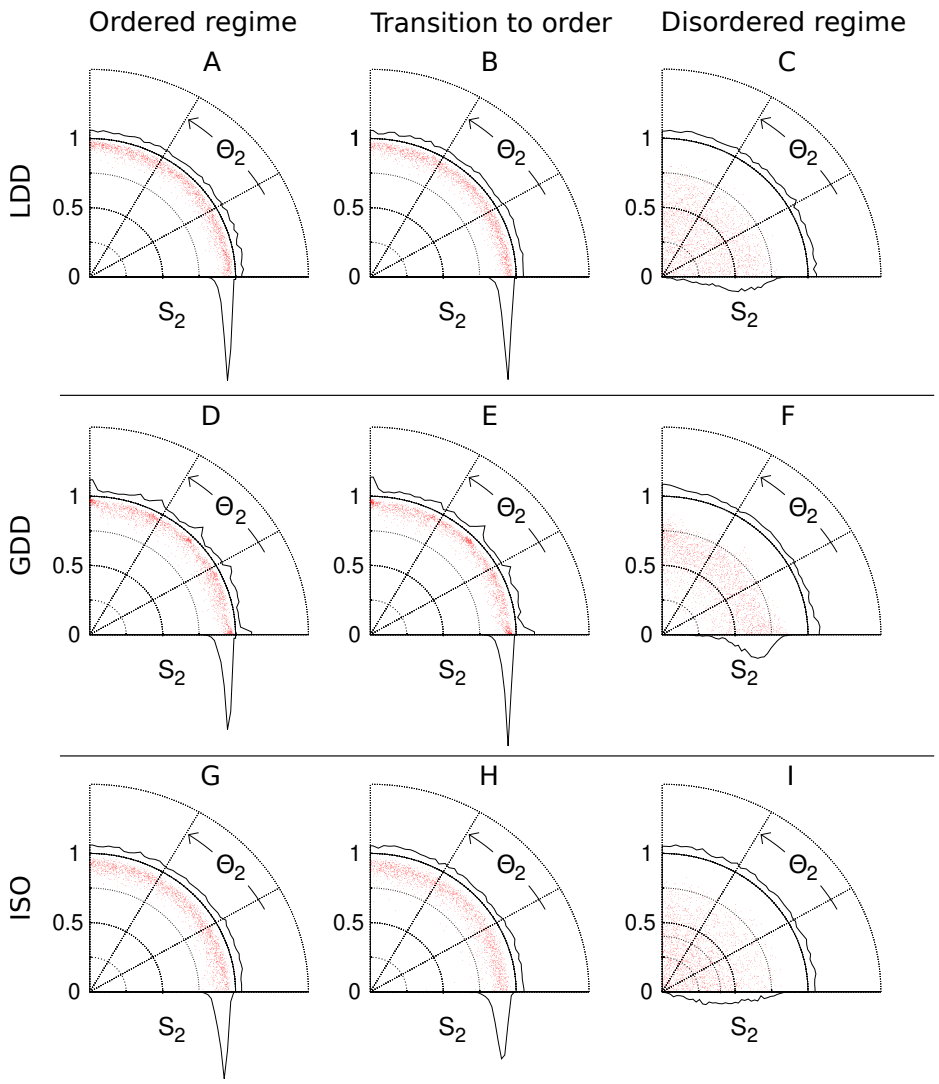

Figure 5: Distribution of S_2 and Θ_2 for three different regimes. Each panel contains the result in terms of alignment S_2 and orientation Θ_2 of 2000 independent runa at $T = 3 \times 10^4$ sec. A point located along the horizontal axis represents a perfectly transverse array orientation, while a point on the vertical axis represents a perfectly longitudinal orientation. The distance of the point from the origin indicates the strength of the alignment, with greater distances indicating a higher degree of alignment. The data points are collected to generate histograms for the distribution of S_2 (horizontal axis) and Θ_2 (vertical axis). G values: (A) $G = -0.22$, (B) $G = -0.25$, (C) $G = -0.42$, (D) $G = -0.23$, (E) $G = -0.25$, (F) $G = -0.54$, (G) $G = -0.16$, (H) $G = -0.18$, (I) $G = -0.25$. Panels (A), (D), and (G) correspond to the empty markers of Figure 4A.

Figure 5 shows the distribution of both order parameters S_2 and Θ_2 over 2000 simulation runs for LDD (Figure 5A-C), GDD (Figure 5D-F), and ISO (Figure 5G-I), each for three different values of

the parameter G that correspond to aligned array (Figure 5A, D, and G), transition to fully aligned array (Figure 5B, E, and H), and disordered array (Figure 5C, F, and I). As we would expect, in the case of LDD and ISO nucleation, the distribution of Θ_2 after $T = 3 \times 10^4$ sec was uniform for each of the three G values. On the contrary, in the case of GDD nucleation, computational artefacts arose. Indeed, Figure 5D shows five preferential alignments for an ordered array: $\Theta_2 = 0$, $\Theta_2 = \pi/8$, $\Theta_2 = \pi/4$, $\Theta_2 = 3\pi/8$, and $\Theta_2 = \pi/2$, see Figure 5D. The $\Theta_2 = 0$ and $\Theta_2 = \pi/2$ alignments are due the presence of bundles that wrapped around themselves along the shortest possible path. This effect, which should be in principle visible for LDD and ISO too, was only recorded in the GDD case due to the inhomogeneity problem, i.e., the presence of few highly populated and, therefore, very long, bundles. The remaining three preferred orientations at $\Theta_2 = \pi/8$, $\Theta_2 = \pi/4$, $\Theta_2 = 3\pi/8$ are a computational artefact due to the subdivision of the simulation domain in small square grid cells, with the consequence of more likely selecting as parent microtubules those that were aligned along the (anti-)diagonal of such square grids, or even the combination of two adjacent square grids. For slightly lower interaction strength, i.e., lower G (Figure 5E), only $\Theta_2 = 0$, $\Theta_2 = \pi/4$, and $\Theta_2 = \pi/2$ preferred orientation survived. Though this bias was relatively small, it could be relevant when one wants to study the response of the array as a whole to small directional cues.

Note that, in the disordered state, LDD and ISO lead to similar distributions for both S_2 and Θ_2, where the former tended to be relatively flat and the latter was very uniform, especially when compared to the GDD scenario. In GDD, the preferred orientations of $\Theta_2 = 0$ and $\Theta_2 = \pi/2$ were somewhat preserved, and S_2 exhibits peaks in the distribution at average values, as shown in Figure 5C, F, and I. This phenomenon could be attributed to LDD primarily involving unbound nucleation at low G values, at which point the microtubule density was average. In contrast, GDD continued to support a significant amount of microtubule-based nucleation, which had the capability to form densely packed bundles.

Local and global density-dependence emerge from LDD nucleation

To verify that our proposed LDD nucleation mode exhibits density-dependence in the probability of microtubule-based nucleation, we computed the fraction of such nucleation events relative to the total number of nucleation events as a function of the density of microtubule length per unit of area. This assessment was conducted at both local and global scales. The global microtubule density was computed using the formula $\rho = \sum_i l_i/A$, where l_i represents the length of the i-th microtubule, the summation runs over all microtubules, and A denotes the area of the simulation domain. Instead, the local tubulin density was determined by the formula $\rho = \sum_{i,j} l_{i_j} / \sum_j A_j$. In this expression, l_{i_j} represents the length of the segment of the i-th microtubule within region j with area A_j, and j runs over all regions touched by the metatrajectories drawn from the insertion location of a nucleation complex, as shown by the schematic in Figure 6A.

Figure 6 shows that density-dependence of microtubule-based nucleation naturally emerged from LDD mode without being imposed by Equation (1) as in the GDD case. This density-dependence behaviour was maintained across local and global scale. We fitted the data from our simulations by superimposing the fitting function $\rho/(\rho + a)$ and we obtained $a = 0.19 \pm 0.01$ for the local microtubule density (Figure 6A), and $a = 0.18 \pm 0.01$ for the global microtubule density (Figure 6B).

Note that, at high microtubule density ($\rho \simeq 5\mu\text{m}^{-1}$), the frequency of occurrence of microtubule-based nucleation remained below 1, specifically around 0.95 for high local density (as shown in Figure 6A) and 0.9 for high global density (Figure 6B). These frequencies were lower than the experimentally measured value of approximately 0.98 by Nakamura et al. [14]. This discrepancy

could arise from the fact that, in our simulations, we did not consider that nucleation complexes appear at the membrane preferentially in the vicinity of microtubule lattices [11, 12], which would lead to a higher likelihood of microtubule-based nucleation. Consequently, our algorithm slightly underestimated the frequency of occurrence of microtubule-based nucleation events.

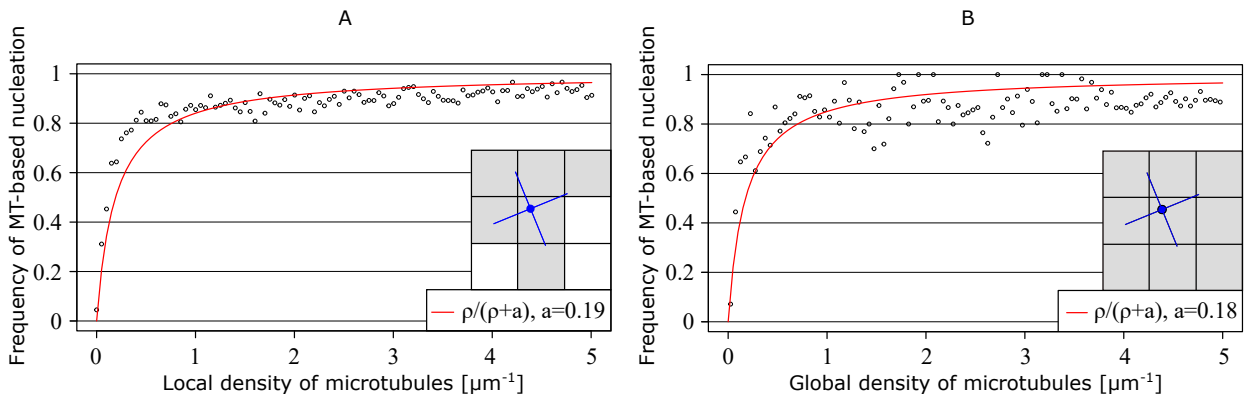

Figure 6: Frequency of microtubule-based nucleation as a function of (A) local and (B) global density of microtubules for a simulation run. In this simulation, $r_c = 0.0025$ sec^{-1}.

Geometrical effects on the orientation of alignment

We tested how our algorithm influenced array alignments within more complex and realistic cellular geometries by running simulations on two cylindrical domains. These domains maintained a constant height-to-diameter ratio while varying the overall dimensions of the cylinders. We incorporated two distinct directional biases independently: a global bias, represented by a 8% increase in the catastrophe rate at the cylinder caps, and a local bias, with a maximum 8% directional enhancement in the rescue rate for individual microtubules. Mathematically, the adjustment in the rescue rate is expressed as:

$$r_{r,\text{extra}} = \frac{b_{\max}}{2}\left[1 + \cos\left(2(\theta - \theta_r)\right)\right], \tag{10}$$

where θ denotes the shrinkage direction of the microtubule plus end, θ_r represents the angle at which the rescue rate is maximum, and $b_{\max} = 0.08$ is the maximal increase factor when $\theta = \theta_r$.

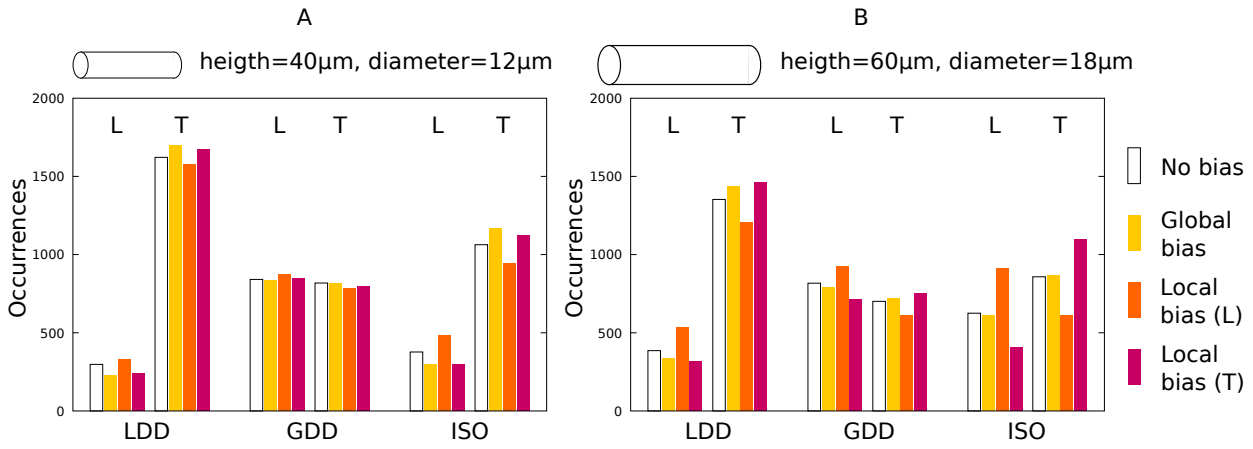

Figure 7: Number of aligned arrays at $T = 3 \times 10^4$ sec in the transverse (T, when $-10° < \Theta_2 < 10°$), or longitudinal (L, when $80° < \Theta_2 < 100°$) direction, with directional biases. The simulation domain is a cylinder of (A) 40μm length and 12μm diameter, and (B) 60μm length and 18μm diameter.

Figure 7 shows the frequency of alignment in both longitudinal ($80° < \Theta_2 < 100°$) and transverse ($-10° < \Theta_2 < 10°$) orientations across 2000 simulation runs for the three nucleation modes and different orientational biases. The LDD method exhibited a pronounced preference for transverse alignment over longitudinal. This preference could be explained by the formation of "bracelets" of microtubule bundles that wrapped around themselves, as shown in Figure S5B. In a smaller cylindrical domain, more than 75% of the simulations resulted in a transverse orientation of the microtubule arrays. This outcome was consistent regardless of the incorporation of global or local biases (Figure 7A). For larger simulation domains (Figure 7B), a strong inclination towards transverse orientation remained evident. However, in the latter case, slight directional biases favouring longitudinal orientation slightly increased the instances of longitudinal array formations, though less frequently than transverse arrays. The observed phenomenon likely stemmed from the extended trajectories required by transverse bundles to complete their self-wrapping process, which marginally promoted the emergence of local ordering in other directions than transverse

Figure 7A also shows that in smaller simulation domains, the GDD nucleation mode did not exhibit a preference for either orientation, with minor directional signals (both global and local) having little impact on establishing a preferred alignment. This observation is related to intense competition among initially forming aligned arrays, which predominantly consisted of one or two densely populated bundles, as shown in Figure S5A. Surprisingly, in larger cylindrical domains, we observed a slight predisposition towards longitudinal orientation over transverse orientation. This can be understood by noting that slight deviations from a transverse orientation can be detrimental for the stability of densely populated bundles. When these bundles are excessively long, i.e., when they reach the cap of the cylinder and return back with mirrored orientation, they risk colliding with themselves, with individual microtubules in the bundle undergoing induced catastrophes, potentially causing initial transverse bundles to be outcompeted by initially longitudinal bundles (Figure S5A). These longitudinal bundles, in contrast, benefit from the topology of the simulation domain, offering them greater stability against minor deviations relative to the longitudinal direction. Similar to the LDD scenario, both global and local cues appeared to have a more pronounced influence in determining orientation in larger domains compared to smaller ones.

When nucleation occurred isotropically, the addition of directional biases had a more significant effect on the preferred orientation of the cortical array than observed with the LDD and GDD modes. This effect was particularly evident in larger simulation domains, where a local directional bias could effectively determine the preferred orientation of the cortical array, as shown in Figure 7B and in line with previous results [18].

Discussion

In this work, we have developed a novel, computational time efficient nucleation algorithm for realistic microtubule bound nucleation that does not suffer from the inhomogeneity problem that haunted the field for over a decade [11,12,21,28]. We showed that different nucleation algorithms can have great impact on the overall behaviour of the cortical array. In particular, microtubule-based nucleation with local density-dependence to microtubule density extended the length and life time of microtubule bundles, thereby increasing the regime of spontaneous alignment and making the array more sensitive to subtle orientational cues from the cell's geometry. The ability to simulate this force realistically, opens up the possibility of quantitative comparison of different forces acting on array orientation.

The orientation of the cortical array within cellular structures is influenced by different forces, both global and local. Global cues, such as the inherent geometry of the cell, play a crucial role in predisposing an aligned array towards specific orientations that correlate with the shortest closed circumferences [5, 16], indicating the existence of a selection process for certain orientations based on cellular geometry. Specific cues like penalties for crossing (sharp) edges [36] or cell faces with less favourable conditions can further restrict the subset of realized alignments. Besides geometry, also mechanical and developmental signals can trigger the cell to select a different orientation of this limited set [17, 37–39]. On the other hand, local cues also play a significant role in determining the orientation of the cortical array. A striking example of this is the alignment of cortical microtubules with mechanical stresses in the cell wall, facilitated by mechanisms that are currently not fully understood but are believed to involve the mediation of katanin severing [17, 25, 40, 41]. This phenomenon shows how microtubules can co-align with mechanical stresses, potentially through a bias in microtubule dynamics that favors the growth of microtubules in a particular orientation [18, 19, 40, 42]. The development of a more realistic nucleation algorithm, as we proposed with our local density-dependent nucleation mode, offers a promising avenue for quantitatively exploring the interplay between these local and global orienting forces.

The observation that realistic models for microtubule-based nucleation apply a significant bias towards alignment in the transverse direction in cylindrical cells presents an intriguing contrast to previous theoretical works. Indeed, it has been proposed that a longitudinal alignment minimizes the bending energy of individual microtubules, especially in the context of infinitely long cylinders [43,44]. Whether this advantage is sufficient to cause individual microtubules to deviate from a transverse to a longitudinal orientation likely depends on the density and speed with which they are anchored to the plasma membrane [43, 45]. In this study, we focused on the impacts of topology and minor dynamic biases, without delving into the interactions between these factors and mechanical or developmental constraints. Future theoretical and computational works should aim to link the impact of cell topology and the mechanical stresses induced by geometry on individual microtubules with the preferred orientations of the aligned cortical array as a whole.

The criticality of nucleation in determining specific directions for alignment suggests that

even minor predispositions at the nucleation phase can lead to substantial differences in the final orientation of the array, highlighting the sensitivity of the system to initial conditions. The fact that an initial small preferred orientation of alignment could significantly influence the selection of persistent orientation angles, as in the case of GDD, raises important questions about the practical relevance of non-realistic nucleation modes when simulating microtubule dynamics on realistic cell shapes. In this light, introducing additional considerations, such as microtubule flexibility is essential, particularly because the effects of geometry and other global cues may be nuanced by the actual persistence length of microtubules [18, 24]. Such a persistence length, indeed, can restrict how far local signals can be transmitted through the array, which is critical for understanding the limitations of information propagation within the microtubule network.

Our algorithm, designed for bias-free, computationally efficient, and realistic simulation of microtubule nucleation, has potential implications for modelling anisotropic cell expansion and organ bending when the orientation of the alignment of the cortical array is different than transverse [46], e.g., in the case of helical microtubule arrays as observed in *Arabidopsis thaliana* mutants [38, 47–50]. The underlying physical mechanisms behind such an helicity in the cortical array remain elusive. By enhancing biological realism, our nucleation algorithm offers a novel method to study possible mechanisms behind such an helical growth, by more realistically nuancing the interplay between global cues due to cell geometry and local biases at the level of the dynamics of individual microtubules. Previous implementation of microtubule-based nucleation [21, 28], as in the GDD case in this work, posses lower informative power as the final alignment of an array, by strongly depending on any initial emerging orientation due the positive feedback that attracts new nucleations in the same direction of extant microtubules, minimises the impact of biases. Conversely, we showed that isotropic nucleation was more susceptible to local and global biases, in agreement with previous research [15, 18], with the risk to exaggerate small imbalances that, in a real situation, would be irrelevant for the final array orientation.

Our algorithm reveals that nucleation modality significantly influences the selection of a specific orientation in more realistic cell shapes, like capped cylinders. This makes it ideal for simulations of cortical microtubules that aim to explore the impact of minor directional biases and interaction between cell topology and mechanical or developmental constaints on the alignment and the orientation of the array as a whole.

References

[1] Ehrhardt DW, Shaw SL. Microtubule dynamics and organization in the plant cortical array. Annual Review of Plant Biology. 2006;57:859–75.

[2] Sablowski R. Coordination of plant cell growth and division: collective control or mutual agreement? Current Opinion in Plant Biology. 2016;34:54–60.

[3] Wasteneys GO. Microtubule organization in the green kingdom: chaos or self-order? Journal of Cell Science. 2002;115:1345.

[4] Chan J, Coen E. Interaction between autonomous and microtubule guidance systems controls cellulose synthase trajectories. Current Biology. 2020;30(5):941–947.

[5] Chakrabortty B, Willemsen V, de Zeeuw T, Liao CY, Weijers D, Mulder B, et al. A plausible microtubule-based mechanism for cell division orientation in plant embryogenesis. Current Biology. 2018;28(19):3031–3043.

[6] Gutierrez R, Lindeboom JJ, Paredez AR, Emons AM, Ehrhardt DW. Arabidopsis cortical microtubules position cellulose synthase delivery to the plasma membrane and interact with cellulose synthase trafficking compartments. Nature Cell Biology. 2009;11(7):797–806.

[7] Paredez AR, Somerville CR, Ehrhardt DW. Visualization of Cellulose Synthase Demonstrates Functional Association with Microtubules. Science. 2006;312(5779):1491–1495.

[8] Tindemans SH, Hawkins RJ, Mulder BM. Survival of the aligned: ordering of the plant cortical microtubule array. Phys Rev Lett. 2010;104(5):058103.

[9] Deinum EE, Mulder BM. Modelling the role of microtubules in plant cell morphology. Curr Opin Plant Biol. 2013;16(6):688–692.

[10] Dixit R, Cyr R. Encounters between Dynamic Cortical Microtubules Promote Ordering of the Cortical Array through Angle-Dependent Modifications of Microtubule Behavior. The Plant Cell. 2004;16(12):3274–3284.

[11] Jacobs B, Schneider R, Molenaar J, Filion L, Deinum EE. Microtubule nucleation complex behavior is critical for cortical array homogeneity *and* xylem wall patterning. Proceedings of the National Academy of Sciences. 2022;119(50):e2203900119.

[12] Schneider R, Klooster Kv, Picard KL, van der Gucht J, Demura T, Janson M, et al. Long-term single-cell imaging and simulations of microtubules reveal principles behind wall patterning during proto-xylem development. Nature communications. 2021;12(1):1–12.

[13] Sambade A, Pratap A, Buschmann H, Morris RJ, Lloyd C. The influence of light on microtubule dynamics and alignment in the Arabidopsis hypocotyl. Plant Cell. 2012;24(1):192–201.

[14] Nakamura M, Ehrhardt DW, Hashimoti T. Microtubule and katanin-dependent dynamics of microtubule nucleation complexes in the acentrosomal Arabidopsis cortical array. Nature Cell Biology. 2010;12(11):1064–70.

[15] Chakrabortty B, Blilou I, Scheres B, Mulder BM. A computational framework for cortical microtubule dynamics in realistically shaped plant cells. PLoS computational biology. 2018;14(2):e1005959.

[16] Deinum EE, Mulder BM. Modelling the Plant Microtubule Cytoskeleton. In: Morris RJ, editor. Mathematical Modelling in Plant Biology. Springer; 2018. p. 53–67.

[17] Hamant O, Heisler MG, Jonsson H, Krupinski P, Uyttewaal M, Bokov P, et al. Developmental patterning by mechanical signals in Arabidopsis. Science. 2008;322(5908):1650–5.

[18] Mirabet V, Krupinski P, Hamant O, Meyerowitz EM, Jönsson H, Boudaoud A. The self-organization of plant microtubules inside the cell volume yields their cortical localization, stable alignment, and sensitivity to external cues. PLoS computational biology. 2018;14(2):e1006011.

[19] Saltini M, Mulder BM. A plausible mechanism for longitudinal lock-in of the plant cortical microtubule array after light-induced reorientation. Quantitative Plant Biology. 2021;2:e9.

[20] Chan J, Sambade A, Calder G, Lloyd C. Arabidopsis Cortical Microtubules Are Initiated along, as Well as Branching from, Existing Microtubules. Plant Cell. 2009;12(8):2298–306.

[21] Deinum EE, Tindemans SH, Mulder BM. Taking directions: the role of microtubule-bound nucleation in the self-organization of the plant cortical array. Phys Biol. 2011;8(5):056002.

[22] Foteinopoulos P, Mulder BM. The effect of anisotropic microtubule-bound nucleations on ordering in the plant cortical array. Bulletin of mathematical biology. 2014;76(11):2907–2922.

[23] Hawkins T, Mirigian M, Yasar MS, Ross JL. Mechanics of microtubules. Journal of biomechanics. 2010;43(1):23–30.

[24] Durand-Smet P, Spelman TA, Meyerowitz EM, Jönsson H. Cytoskeletal organization in isolated plant cells under geometry control. Proceedings of the National Academy of Sciences. 2020;117(29):17399–17408.

[25] Colin L, Chevallier A, Tsugawa S, Gacon F, Godin C, Viasnoff V, et al. Cortical tension overrides geometrical cues to orient microtubules in confined protoplasts. Proceedings of the National Academy of Sciences. 2020;.

[26] Gomez JM, Chumakova L, Bulgakova NA, Brown NH. Microtubule organization is determined by the shape of epithelial cells. Nature Communication. 2016;7:13172.

[27] Murata T, Sonobe S, Baskin TI, Hyodo S, Hasezawa S, Nagata T, et al. Microtubule-dependent microtubule nucleation based on recruitment of gamma-tubulin in higher plants. Nature Cell Biology. 2005;7(10):961–8.

[28] Allard JF, Wasteneys GO, Cytrynbaum EN. Mechanisms of self-organization of cortical microtubules in plants revealed by computational simulations. Molecular Biology of the Cell. 2010;21(2):278–86.

[29] Eren EC, Dixit R, Gautam N. A 3D Computer Simulation Model Reveals the Mechanisms for Self-Organization of Plant Cortical Microtubules into Oblique Arrays. Mol Biol Cell. 2010;21(15):2674–84.

[30] Motta MR, Nedelec F, Woelken E, Saville H, Jacquerie C, Pastuglia M, et al. The cell cycle controls spindle architecture in Arabidopsis by modulating the augmin pathway. bioRxiv. 2023; p. 2023–11.

[31] Tindemans SH, Deinum EE, Lindeboom JJ, Mulder B. Efficient event-driven simulations shed new light on microtubule organisation in the plant cortical array. Frontiers in Physics. 2014;2(19):9.

[32] Deinum EE, Tindemans SH, Lindeboom JJ, Mulder BM. How selective severing by katanin promotes order in the plant cortical microtubule array. Proceedings of the National Academy of Sciences. 2017;114(27):6942–6947.

[33] Dogterom M, Leibler S. Physical aspects of the growth and regulation of microtubule structures. Physical Review Letters. 1993;70:1347.

[34] Shaw SL, Kamyar R, Ehrhardt DW. Sustained Microtubule Treadmilling in Arabidopsis Cortical Arrays. Science. 2003;300(5626):1715–1718.

[35] Schmit AC. Acentrosomal microtubule nucleation in higher plants. International Review of Cytology. 2002;220:257–89.

[36] Ambrose C, Allard JF, Cytrynbaum EN, Wasteneys GO. A CLASP-modulated cell edge barrier mechanism drives cell-wide cortical microtubule organization in *Arabidopsis*. Nature Communication. 2011;2:430.

[37] Lindeboom JJ, Nakamura M, Hibbel A, Shundyak K, Gutierrez R, Ketelaar T, et al. A mechanism for reorientation of cortical microtubule arrays driven by microtubule severing. Science. 2013;342(6163):1245533.

[38] Nakamura M, Lindeboom JJ, Saltini M, Mulder BM, Ehrhardt DW. SPR2 protects minus ends to promote severing and reorientation of plant cortical microtubule arrays. Journal of Cell Biology. 2018;217(3):915–927.

[39] Lindeboom JJ, Nakamura M, Saltini M, Hibbel A, Walia A, Ketelaar T, et al. CLASP stabilization of plus ends created by severing promotes microtubule creation and reorientation. Journal of Cell Biology. 2019;218(1):190–205.

[40] Uyttewaal M, Burian A, Alim K, Landrein B, Borowska-Wykret D, Dedieu A, et al. Mechanical stress acts via katanin to amplify differences in growth rate between adjacent cells in *Arabidopsis*. Cell. 2012;149:439.

[41] Sampathkumar A, Krupinski P, Wightman R, Milani P, Berquand A, Boudaoud A, et al. Subcellular and supracellular mechanical stress prescribes cytoskeleton behavior in Arabidopsis cotyledon pavement cells. Elife. 2014;3:e01967.

[42] Louveaux M, Julien JD, Mirabet V, Boudaoud A, Hamant O. Cell division plane orientation based on tensile stress in *Arabidopsis thaliana*. Proceedings of the National Academy of Science. 2016;113:E4294.

[43] Bachmann S, Froese R, Cytrynbaum EN. A buckling instability and its influence on microtubule orientation in plant cells. SIAM Journal on Applied Mathematics. 2019;79(5):2132–2149.

[44] Lagomarsino MC, Tanase C, Vos JW, Emons AMC, Mulder BM, Dogterom M. Microtubule Organization in Three-Dimensional Confined Geometries: Evaluating the Role of Elasticity Through a Combined In Vitro and Modeling Approach. Biophysical Journal. 2007;92(3):1046.

[45] Tian TY, Macdonald CB, Cytrynbaum EN. A stochastic model of cortical microtubule anchoring and mechanics provides regulatory control of microtubule shape. Bulletin of Mathematical Biology. 2023;85(11):1–23.

[46] Buschmann H, Borchers A. Handedness in plant cell expansion: a mutant perspective on helical growth. New Phytologist. 2020;225:53–56.

[47] Ishida T, Kaneko Y, Iwano M, Hashimoto T. Helical microtubule arrays in a collection of twisting tubulin mutants of Arabidopsis thaliana. Proceedings of the National Academy of Science. 2007;104(20):8544–9.

[48] Buschmann H, Sambade A, Pesquet E, Calder G, Lloyd CW. Microtubule Dynamics in Plant Cells. In: Methods in Cell Biology. Elsevier; 2009.

[49] Nakamura M, Hashimoto T. A mutation in the Arabidopsis gamma-tubulin-containing complex causes helical growth and abnormal microtubule branching. Journal of Cell Science. 2009;122:2208–17.

[50] Furutani I, Watanabe Y, Prieto R, Masukawa M, Suzuki K, Naoi K, et al. The *SPIRAL* genes are required for directional control of cell elongation in *Arabidopsis thaliana*. Development. 2000;127:4443–53.

Supplementary Figures

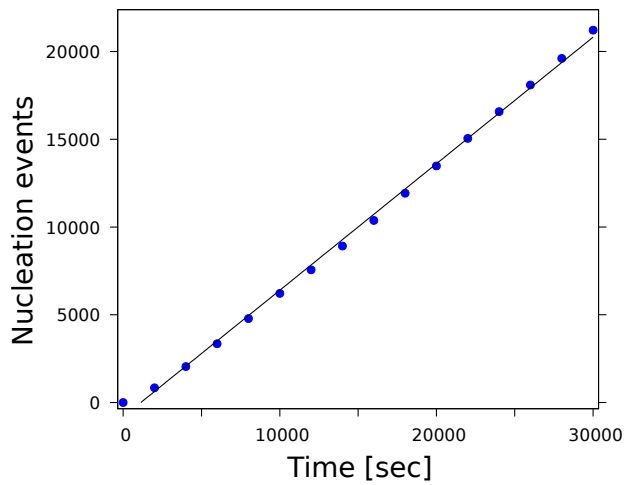

Figure S1: Cumulative number of nucleation events as a function of time for one simulation run with LDD nucleation mode and in a square simulation domain with periodic boundary conditions and size $L = 40\mu$m. The black line corresponds to the fitting function $f(t) = a + bt$, with $a = -809 \pm 153$ and $b = 0.72 \pm 0.01$. In this simulation, $r_c = 0.0025$ sec^{-1}.

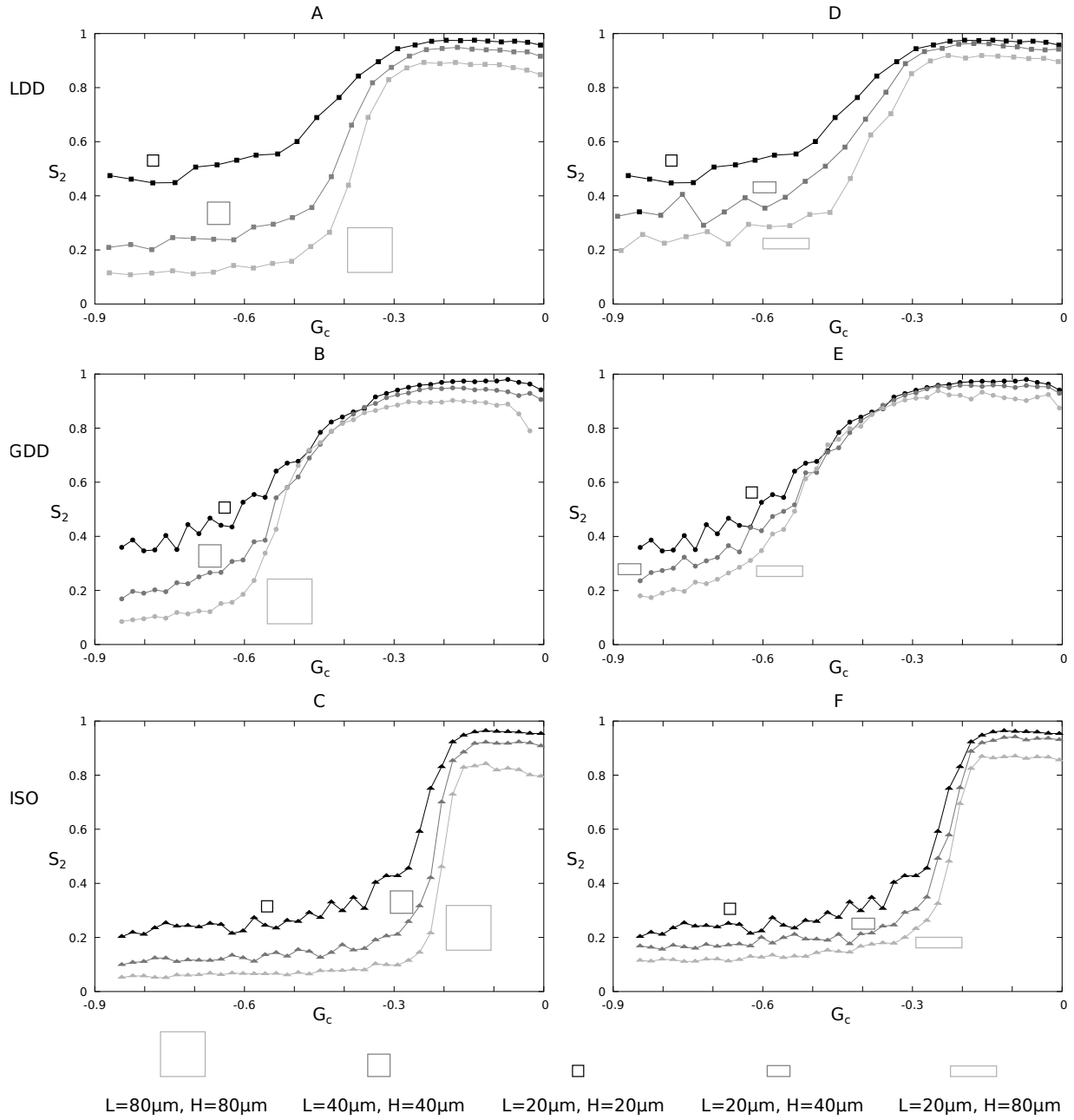

Figure S2: Degree of alignment S_2 as a function of the control parameter G for LDD, GDD, and ISO nucleation modes for (A-C) increasing size and (D-F) increasing height-to-length aspect ratio of the planar simulation domain.

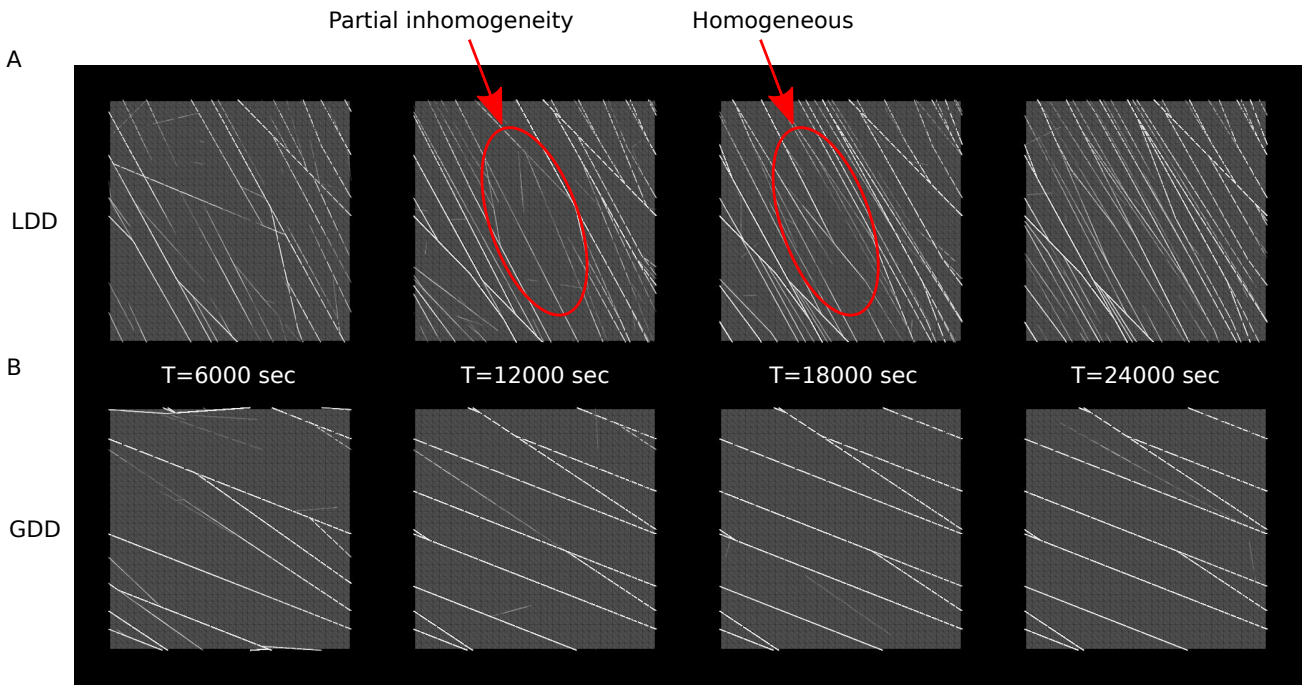

Figure S3: Snapshot of the simulated cortical array for (A) LDD and (B) GDD nucleation modes at four different time stamps. Ellipse in A indicate a region of initially low density where density increases over time. Simulation domain: grid $L = 40\mu$m, $H = 40\mu$m. $r_c = 0.0025$ s^{-1}.

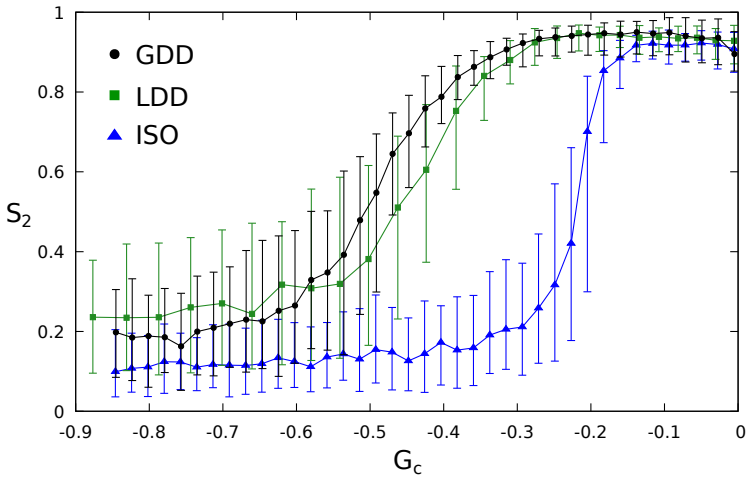

Figure S4: Order parameter S_2 as function of the control parameter G at $T = 3 \times 10^4$ sec, for LDD, GDD, and ISO nucleation modes in a squared geometry with sizes $L = 40\mu$m and $H = 40\mu$m, as depicted in Figure 4. Results are averaged over 100 independent simulation runs, and error bars represent the 10th and 90th percentile.

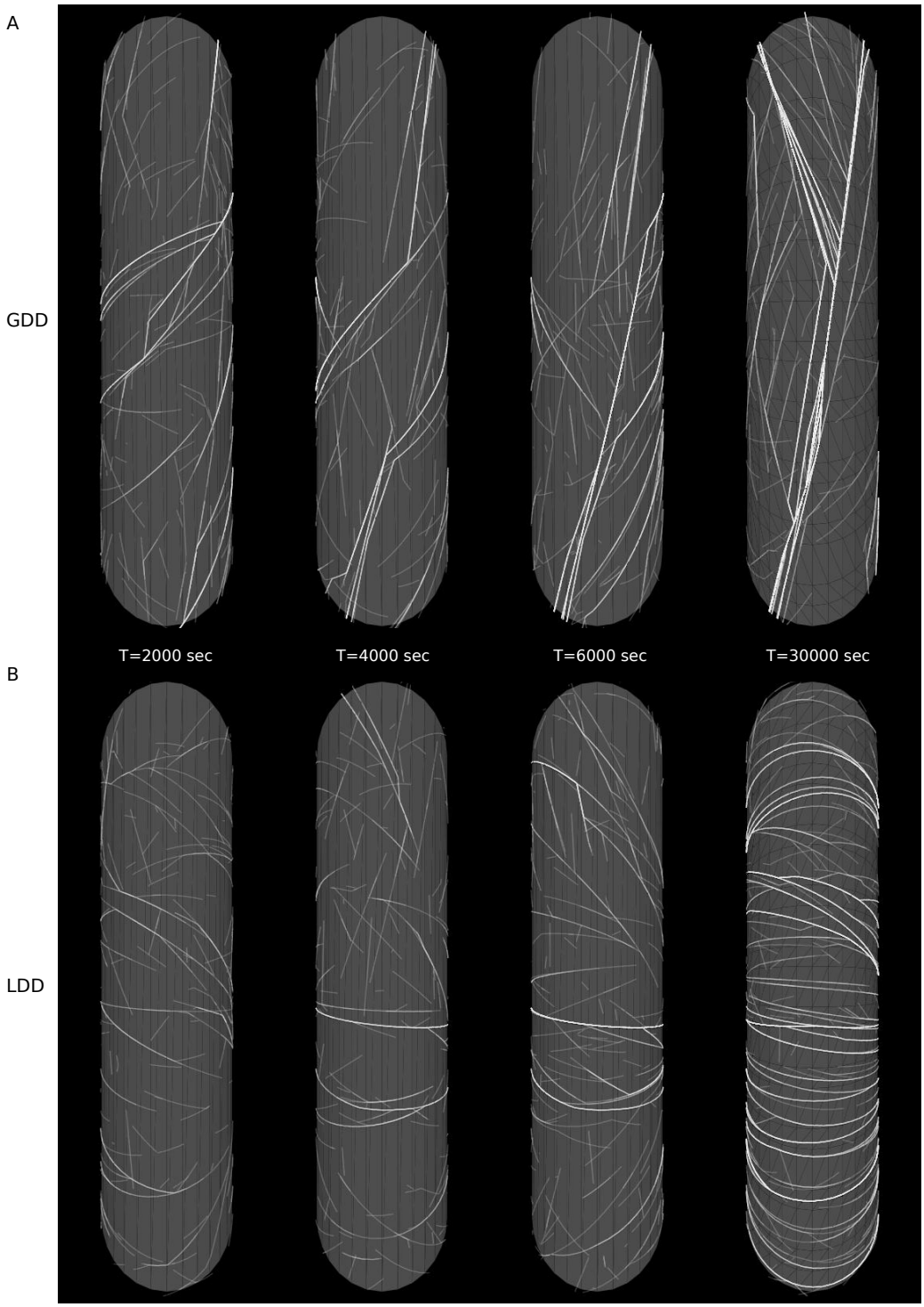

Figure S5: Snapshot of the simulated cortical array for (A) LDD and (B) GDD nucleation modes at four different time stamps. Simulation domain: cylinder with $L = 40\mu$m, diameter= 40μm. In these simulations: $r_c = 0.0025$ s^{-1}.